Highly-sensitive SERS detection of tetracycline: Sub-enhancement brought by light scattering of nano-diamond

Jingxuan Pei, Zhenfei Tian, Xiang Yu, Shuting Zhang, Shiqing Ma, Yibo Sun, Rabah Boukherroub

Highly-Sensitive SERS Detection of Tetracycline: Sub-enhancement Brought by Light Scattering of Nano-diamond

Jingxuan Pei[a, †], Zhenfei Tian[a, †], Xiang Yu[a, *], Shuting Zhang[a], Shiqing Ma[a], Yibo Sun[a], Rabah Boukherroub[b, *]

[a] Beijing Key Laboratory of Materials Utilization of Nonmetallic Minerals and Solid Wastes, National Laboratory of Mineral Materials, School of Materials Science and Technology, China University of Geosciences (Beijing), 29 Xueyuan Road, Haidian, Beijing 100083, China.

[b] Univ. Lille, CNRS, Centrale Lille, ISEN, Univ. Valenciennes, UMR 8520, IEMN, F-59000, Lille, France.

[†] Those authors contributed equally to this work.

[*] Corresponding authors.

E-mail addresses:

yuxiang@cugb.edu.cn; rabah.boukherroub@univ-lille.fr

Abstract

Antibiotic residues in wastewater cause a serious threat to aquatic environment and human safety, and the development of robust strategies for detecting antibiotic residues becomes critical. In this work, a surface-enhanced Raman scattering (SERS) substrate, consisting of gold nanoparticles/nano diamond/carbon nitride (Au/ND/C_3N_4) hybrid, which features enhanced light utilization and self-cleaning properties, is developed for sensitive sensing of tetracycline. The fabricated Au/ND/C_3N_4 substrate effectively captures target molecules and enhances Raman activities, owing to abundant functional groups and light scattering effect of ND. Moreover, the heterostructure formed by Au NPs, ND and C_3N_4 endows this SERS substrate with superior self-cleaning capability, enabling its reusability. The Au/ND/C_3N_4 substrate exhibits high sensitivity (10^{-14} M), desirable reproducibility (RSD=13.29%, n=238) and favourable stability (84.8% of initial intensity after 30 days) for crystal violet probe. Also, no significant loss of SERS or catalytic activity is observed during cyclic SERS detection. Likewise, the detection of tetracycline at nanomolar level and cyclic SERS measurement jointly reveals its prospect for recyclable detection of tetracycline. This work proposes a distinctive strategy for enhancing SERS activity, and the developed self-cleaning Au/ND/C_3N_4 substrate represents a potential candidate for highly sensitive detection of antibiotic residues in wastewater.

Key words: Surface-enhanced Raman scattering; nano diamond; sub-enhancement; sensing; tetracycline

1. Introduction

An increasing concern on monitoring antibiotic residues in wastewater urges the development of high-sensitivity and cost-effective analytical tools to curb environmental pollution. The overuse and delayed metabolism of antibiotics lead to their inevitable residues in water environment, incurring refractory pollution sources [1-3]. From 2000 to 2015, global per-capita consumption of Watch antibiotics experienced a huge increase of 90.9%, and Access antibiotics featured an increase of 26.2% [4]. As an emerging category of pollutants, antibiotics residues in wastewater could induce the emergence of multi-drug resistance (MDR) microbes, antibiotic resistant bacteria (ARB) and antibiotic resistant genes (ARGs) [5, 6]. Bacteria bred by antibiotic residues may sneak into human body and trigger life-threatening infections. A recent report projected about 10 million deaths per year by 2050 associated with antibiotic resistance [7]. Thereupon, highly-sensitive detection of antibiotic residues in wastewater is becoming more and more imperative for preventing environmental pollution and suppressing production of infectious viruses.

Currently, available methods for the detection of antibiotic residues are mainly involved in colorimetric [8], fluorescent [9], chemiluminescent (CL) [10], electrochemical method [11], and electrochemiluminescence (ECL) [12]. Colorimetric, fluorescent, CL, and electrochemical suffer from the drawbacks of low sensitivity, short life time, labelling required, and cumbersome pre-treatment respectively [13, 14]. ECL exhibits poor reliability due to its easy vulnerability by external environment [13]. Based on its ultra-sensitive features, compatibility with aqueous solution, and label-free detection, SERS casts light on ultra-trace molecular analysis for detecting antibiotics [15-17]. The enhancement of analyte Raman signal is mainly due to local amplification of electromagnetic field from the interaction between the incident laser beam and SERS substrate. Electromagnetic (EM) enhancement and chemical (charge transfer, CT) enhancement are two widely-accepted Raman enhancement mechanisms of SERS substrates [18-20]. Applying nano-semiconductor to load gold

nanoparticles (Au NPs) may acquire satisfactory SERS performance by acting on both EM and CT mechanisms. However, the restrictive effect of scant light utilization on SERS activity of such substrates is seriously ignored.

Au NPs can offer long-range EM enhancement for Raman signals by means of their strong localized surface plasmon resonance (LSPR) [21]. Controlling the Au NPs morphology is regarded as a useful method to enhance Raman signals. Constructing nano-tips and adjusting particle size can form SERS hot spots through two SPR effects of lightning rod effect and resonance coupling effect [22, 23]. Various morphologies of Au NPs like nano-needles, nano-stars, and nano-trees have been fabricated and verified to exhibit high SERS sensitivity [24-26]. A combination of nano-semiconductors and Au NPs may enhance Raman signal through CT effect. The heterostructure formed by nano-semiconductors and Au NPs may accelerate charge transfer to induce analyte polarization, and offer short-range chemical enhancement of Raman signals. ZnO, MoS_2, TiO_2, C_3N_4, etc. have been proven to be suited substrate materials for fabricating high-sensitivity SERS substrates [27]. Among them, C_3N_4 is the most promising candidate due to its strong adsorption capacity and superior electronic conductivity [28-30]. Whereas, available works on Au/C_3N_4 substrate ignores the enhancement effect of light utilization efficiency on SERS activity. Increasing utilization efficient of Raman beam may be an efficacious strategy to improve SERS performance. Exploitation of high laser utilization on Au/C_3N_4 substrates is a worth strategy to further improve its SERS activity.

Adopting effective light utilization to improve SERS performance of Au/C_3N_4 substrate has pivotal matters of finding a suitable light utilization path and revealing its action mechanism. Recent investigations on increasing light absorption efficiency to improve SERS sensitivity focus on the fabrication of light trapping structures [31-34]. A combination of precious metals and special structures such as nano-cavities, nano-spirals, and Si micro-pyramid can achieve superior light trapping effect, and those developed structures generate local electromagnetic enhancement due to resonant cavity effect [35-37]. However, the

heavy reliance of the above-mentioned SERS substrates on high-precision manufacturing processes restricts their wide application. Instead, light scattering effect offers a hopeful avenue to improve light utilization. The introduction of nano-diamond (ND) with high light scattering features into the SERS substrate is expected to implement efficient utilization of Raman laser through a handy process. Moreover, the presence of abundant functional groups on ND surface may act as a powerful tool to capture analyte molecules for improving substrate enrichment capacity. Regretfully, it is rare to see a systematic report about adopting light scattering effect of ND to enhance SERS substrate performances. Here, we proposed a strategy to improve SERS activity by means of light scattering, and fabricated Au/ND/C_3N_4 hybrids for SERS detection of a widely used antibiotic tetracycline. A systematic investigation on the microstructure, optical properties and SERS activities of the designed substrate was conducted to reveal improvement mechanism of ND on SERS performance, promoting its application for the detection of antibiotic residues in wastewater.

In this work, ND/C_3N_4 hybrid with holey structure was fabricated in one step with the help of Z204 catalyst, and Au/ND/C_3N_4 hybrid with heterohedral Au NPs was produced by introduction of active agent cetyltrimethylammonium bromide (CTAB). A systematic characterization was conducted on optical properties, microstructure and chemical features of the prepared samples. SERS performances of Au/ND/C_3N_4 substrate with self-cleaning features was assessed using crystal violet as a probe molecule, as well as its application for tetracycline assay. Consequently, ND improvement mechanism was revealed via both experimental data and finite difference time domain (FDTD) simulation.

2. Experimental

2.1 Reagents: All reagents were of analytical grade. Nitric acid, sulfuric acid, melamine, sodium citrate and CTAB were purchased from Shanghai Aladdin Biochemical Technology Co., Ltd. Crystal violet (CV), tetracycline and chloroauric acid ($HAuCl_4$, 48~50%) were purchased from Shanghai Maclean Biochemical Technology Co., Ltd. Nano-diamonds (~10 nm, 99%) and Z204 catalyst were

purchased from Nanjing Hongde Nanomaterials Co., Ltd. and Sichuan Tianyi Technology Co., Ltd., respectively.

2.2 Characterizations: Optical properties of the prepared samples were investigated by UV-vis diffuse reflectance spectra (Lambda 750, PE). Microtopography and surface element distribution were observed by scanning electron microscopy (SEM, SUPRA55, Zeiss) and transmission electron microscopy (TEM, Talos F200X, ThermoFisher). Element composition and chemical state of Au/ND/C_3N_4 hybrid were determined by X-ray photoelectron spectroscopy (XPS, Escalab 250Xi, ThermoFisher). Phase composition was acquired with an X-ray diffractometer (XRD, D8 Advance, Bruker). Surface functional group composition was assessed with Fourier Transform InfraRed Spectrometer (FT-IR, Specture 100, Peikin Elmer). Surface area were acquired with a specific surface and pore size analyzer (ASAP2020, Micromeritics). Adsorption capacity was investigated by UV-vis absorption spectrophotometry (Lambda 750, PE). SERS performances were recorded by HORIBA Raman microscope (LabRAM HR Evolution, Jobin Yvon; λ_{ex}=633 nm). Photocatalytic experiments were conducted using a photoreactor with a xenon lamp (XE-JY500, Beijing Newbit Technology Co., Ltd.).

2.3 Pre-treatment of ND *Step I*, acid pickling was utilized to remove metal impurities in ND. ND powders (1 g) were dispersed in a mixed solution of nitric acid (5 mL) and sulfuric acid (15 mL), and then the mixture was heated at 40 ^{o}C for 1 h under stirring. Subsequently, the ND were washed with ultrapure water to neutral, and grey ND powder was thus obtained after centrifugation and drying. *Step II*, a heat treatment was carried on ND to decompose the sp^2-C on ND surface. ND powder in *Step I* was calcined at 420 ^{o}C for 1 h to produce purified ND.

2.4 Fabrication of ND/C_3N_4 hybrid. Melamine and purified ND were used as raw materials to prepare ND/C_3N_4 hybrid. A mixture (4 g) of melamine and ND was fully ground (>120 min) and placed in a small crucible, wherein, the mass percentages of ND were set to 1%, 3%, 5%, 7%, and 9%. Afterward, the small crucible was placed in a large crucible containing Z204 catalyst (2 pieces), and the covered crucible was calcined in a muffle furnace. Furnace temperature was raised to 550 ^{o}C at a rate of 5

°C/min, and held for 4 h. The fabricated ND/C_3N_4 hybrid was washed with ultrapure water and then dried and collected. The colour of ND/C_3N_4 hybrid gradually changed from light yellow to brown upon increasing of ND content.

2.5 Fabrication of Au/ND/C_3N_4 hybrid. Gold nanoparticles (Au NPs) loading was accomplished through $HAuCl_4$ reduction with sodium citrate in presence of CTAB to induce overgrowth of Au NPs and produce heterohedral morphology. C_3N_4/ND (20 mg), CTAB (0.11 g) and $HAuCl_4$ solution (1.5 mL, 5 wt%) were dispersed in ultrapure water (17 mL). The resulting mixture was then sonicated for 10 min and stirred for 1 h. The mixture was transferred to a hydrothermal reactor, and sodium citrate solution (0.1 M, 1.5 mL) was added. Thereafter, the reactor was heated and stirred at 110 °C for 5 h. After cooling, the mixture was centrifuged (8000 rpm), and Au/ND/C_3N_4 hybrid was thus collected after drying.

2.6 Photocatalytic activity measurements. Photocatalytic activities of Au/ND/C_3N_4 hybrid were assessed through the degradation of CV and tetracycline. Firstly, the hybrid (50 mg) was immersed in a CV solution (60 mL, 10^{-5} M) and kept in dark for 30 min to ensure the adsorption-desorption equilibrium. Subsequently, the suspension was irradiated under a xenon lamp (500 W). CV absorbance at different time intervals was measured to reflect the photodegradation efficiency. Photodegradation of tetracycline was carried out under the same experimental conditions as for CV, except that the amount of used catalyst was 30 mg. Moreover, photocatalytic activities of pure ND and C_3N_4 were measured under the same condition.

2.7 SERS measurements. Au/ND/C_3N_4 hybrid (20 mg) was mixed with analyte solution (2 mL) for 30 min to ensure sufficient enrichment of target molecules. The mixture was transferred to a silicon wafer and dried for 5 min to form uniform spots (diameter of 4 mm). During the measurement, the laser power and exposure time were respectively set as 5 mW and 5 s.

2.8 Self-cleaning SERS measurements. The Au/ND/C_3N_4 hybrid after SERS investigation was collected, washed with deionized water, and irradiated with a xenon lamp (500 W) for 120 min. After that, it was washed with deionized water and

centrifuged for 2 times to ensure removal of the residues. After drying, the hybrid was collected and applied for another cycle of SERS detection.

3. Results and discussion

3.1. Fabrication and characterization

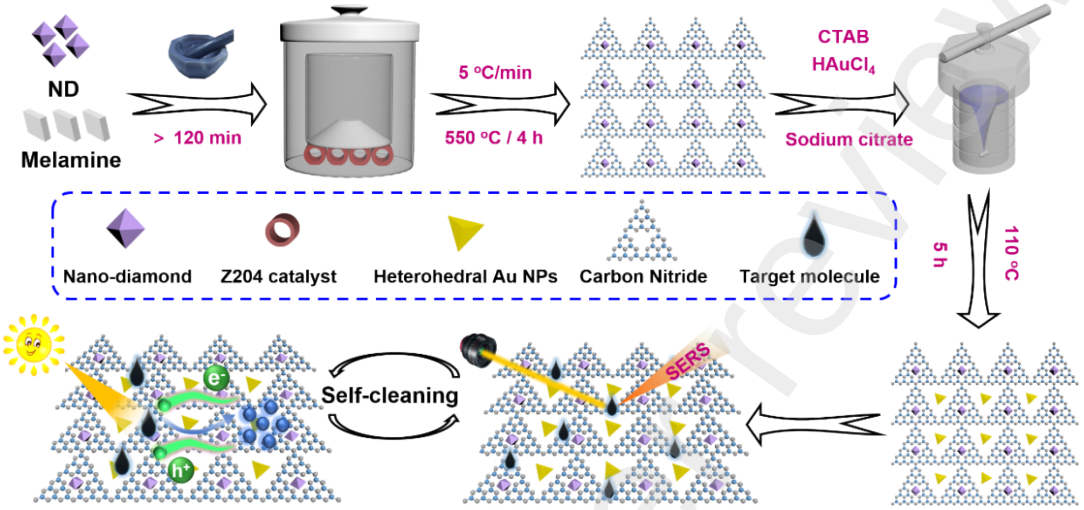

Figure 1. Scheme of the fabrication process and self-cleaning features of the Au/ND/C_3N_4 hybrids

Fig. 1 illustrates the fabrication process and self-cleaning features of the Au/ND/C_3N_4 hybrid. The synthesis of Au/ND/C_3N_4 hybrid includes two steps. Step I, the purified ND (Fig. S1a) with a mean size of ~12 nm was thoroughly mixed with melamine, and the mixture was calcined in presence of Z204 catalyst to produce holey ND/C_3N_4 hybrid (Fig. S1b). Z204 catalyst decomposed ammonia gas (NH_3) generated from thermal polymerization of melamine, and accelerated NH_3 escape to generate cavities [38]. Step II, ND/C_3N_4 hybrid was dispersed into a mixed solution of chloroauric acid and sodium citrate, and a hydrothermal reaction was conducted to synthesize Au/ND/C_3N_4 hybrid with an in-situ loading of Au NPs. In this process, CTAB surfactant was introduced to induce overgrowth of Au NPs, forming heterohedral structures with rich tips. Benefiting from abundant functional groups, π-π conjugate and electrostatic interactions of ND and C_3N_4, the analyte can be quickly and efficiently enriched on Au/ND/C_3N_4 substrate [29, 39]. Moreover, the nano-tips of the heterohedral Au NPs can offer more SERS hot spots, which are beneficial for high detection

sensitivity. After completing SERS detection, Au/ND/C_3N_4 substrate may have a self-cleaning property by means of analyte photodegradation under visible light irradiation.

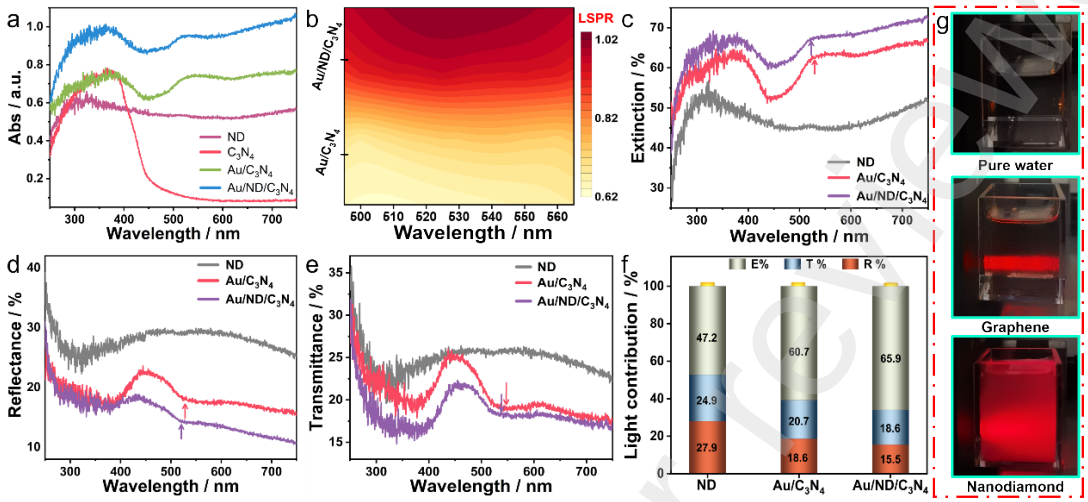

Figure 2. (a) UV-vis diffuse reflectance spectra (DRS) of ND, C_3N_4, Au/C_3N_4 and Au/ND/C_3N_4 hybrid. (b) LSPR intensity contrast of Au/C_3N_4 and Au/ND/C_3N_4. (c-e) Extinction (E), reflectance (R), and transmittance (T) (ERT) spectra of ND, Au/C_3N_4 and Au/ND/C_3N_4 in 250-750 nm region. (f) Light contribution variation of ND, Au/C_3N_4 and Au/ND/C_3N_4. (g) Optical images of pure water, graphene aqueous solution and nanodiamonds aqueous solution under the irradiation of a 633 nm laser.

UV-vis DRS was conducted to investigate the optical properties of samples, as displayed in Fig. 2a. ND exhibits a broad absorption range from 300-700 nm, confirming its positive effect on improving light utilization. C_3N_4 has an absorption edge at ~453 nm, and exhibits a scant light absorption especially in visible range. Au/C_3N_4 behaves an obviously red-shift of absorption edge and enhanced light absorption than that of C_3N_4. A new absorption peak can be observed at 534 nm, assigned to resonance peak of Au NPs. The improved optical properties of Au/C_3N_4 may be ascribed to the strong LSPR effect of Au NPs [40]. For Au/ND/C_3N_4, the absorption edge continues to red-shift and light absorption is further enhanced. In addition, Au NPs absorption peak of Au/ND/C_3N_4 blue-shifts to 531 nm and features a stronger intensity than that of Au/C_3N_4, as shown

in Fig 2b. These results offer direct evidences that the introduction of ND can enhance light utilization and strengthen LSPR effect of plasma in Au/ND/C_3N_4 hybrid.

Subsequently, ERT spectra were determined to assess the light utilization of fabricated samples, wherein E+R+T=100%, as depicted in Fig. 2c-e. ND acquires the highest reflectance than that of Au/C_3N_4 and Au/ND/C_3N_4, indicating its superior light scattering capability (Fig. 2d). In Fig. 2c, the extinction of Au/ND/C_3N_4 exhibits a huge hoist than that of Au/C_3N_4, proving an effective enhancement of ND on light utilization. Moreover, the extinction of Au NPs for Au/C_3N_4 has a resonance peak at~534 nm, while Au/ND/C_3N_4 exhibits the Au NPs resonance peak at~531 nm. The blue-shift of Au NPs resonance peak may be due to the variation of Au NPs morphology and size [41]. Transmittance spectra of ND, Au/C_3N_4 and Au/ND/C_3N_4 are shown in Fig. 2f. In general, the transmittance drop corresponds to the extinction peak position [42]. The transmittance spectra show a blue shift of Au NPs resonance peak as expected. Hereafter, mean ERT are estimated to reflect light contribution variation of ND, Au/C_3N_4 and Au/ND/C_3N_4, as displayed in Fig. 2f. It is apparent that Au/ND/C_3N_4 acquires the highest extinction and is 1.09 times of that Au/C_3N_4. Such enhancement of extinction reveals favourable function of ND on light utilization. Fig. 2g shows the optical images of pure water, graphene aqueous solution and ND aqueous solution under the irradiation of a 633 nm laser. The observed scattered light area in ND aqueous solution illustrates its distinctive light scattering characteristic, different from other carbon materials like graphene. The same results can also be observed in UV-vis spectra of the above samples, as shown in Fig. S2. More commendably, the light-scattering property of ND remains after ND are hybridized with other materials (Fig. S3). Thus, it is reasonable to speculate that the light scattering of ND may improve light utilization of samples for a better SERS activity.

Effect of ND content was further considered on optical properties of Au/ND/C_3N_4 hybrid. Fig. S4 depicts the UV-vis DRS of Au/ND/C_3N_4 hybrids

with five ND contents, as well as resonance peak variation of Au NPs. As shown in Fig. S4, LSPR intensity initially enhances and then lowers with the increase of ND content, and the resonance peak gradually blue-shifts. Au/ND/C_3N_4 hybrid with a ND content of 5% features the strongest resonance peak intensity, and is most promising to acquire superior SERS activity. Fig. S5- Fig.S7 depict the ERT spectra and mean ERT values of the five samples. Au/ND/C_3N_4 hybrid with a ND content of 7% has the biggest extinction, and is slightly higher than that of 5% ND content. Excessive ND content (9%) may induce an increase in reflectance, and reduces the extinction ratio of Au/ND/C_3N_4 hybrid, as shown in Fig. S7.

ND content for Au/ND/C_3N_4 substrate was optimized to acquire a better SERS signal response with crystal violet (CV) probe. Fig. S8 depicts the SERS activity variation of Au/ND/C_3N_4 substrates prepared with five ND contents. The peak at ~1174 cm^{-1}, assigned to C-H in-plane bending mode of CV molecule, is selected as a fingerprint signal of CV [43]. SERS activity initially raises then drops with the increase of ND content. Au/ND/C_3N_4 substrate with 5% ND exhibits the strongest SERS signal. Excess ND content induces an attenuation of the SERS activity due to the strong fluorescence of ND. Considering the optical properties and SERS activity, Au/ND/C_3N_4 with 5% ND is selected as optimal substrate to conduct the following measurements.

TEM was used to observe the microstructure and morphology of the prepared samples. Fig. 3a and Fig. S9 show TEM images of Au NPs with heterohedral morphology. Such heterohedral morphology with nano-tips could enhance EM efficacy by mean of "lightning rod" effect [44]. Micromorphology of ND/C_3N_4 hybrid is depicted in Fig. S1b and Fig. 3b. ND are incorporated into C_3N_4 nanolayers in form of small agglomerates and form strong interactions with C_3N_4 (Fig. S1b). The formation of agglomerates is due to the interaction of abundant functional groups on ND [45]. Different from pure ND (Fig. S1a), ND agglomerates in ND/C_3N_4 hybrid exhibit a smaller mean size. This may be that C_3N_4 acts as a stabilizer and inhibits ND agglomeration during the thermal

polymerization [46]. HRTEM image of ND/C_3N_4 reveals a tight bonding of ND agglomerates with C_3N_4 (Fig. 3b). In Fig. 3b, clear lattice fringes with an interplanar spacing of 0.206 nm can be observed, corresponding to the (111) facet of ND [47]. This provides direct evidence for occurrence of ND on C_3N_4 nanosheets. ND incorporation introduces rigid materials into C_3N_4 stacked layers, expands lamellar spacing of C_3N_4 layers and broadens the nanochannels, which could enhance the enrichment of analyte and accelerate charge transfer during SERS process.

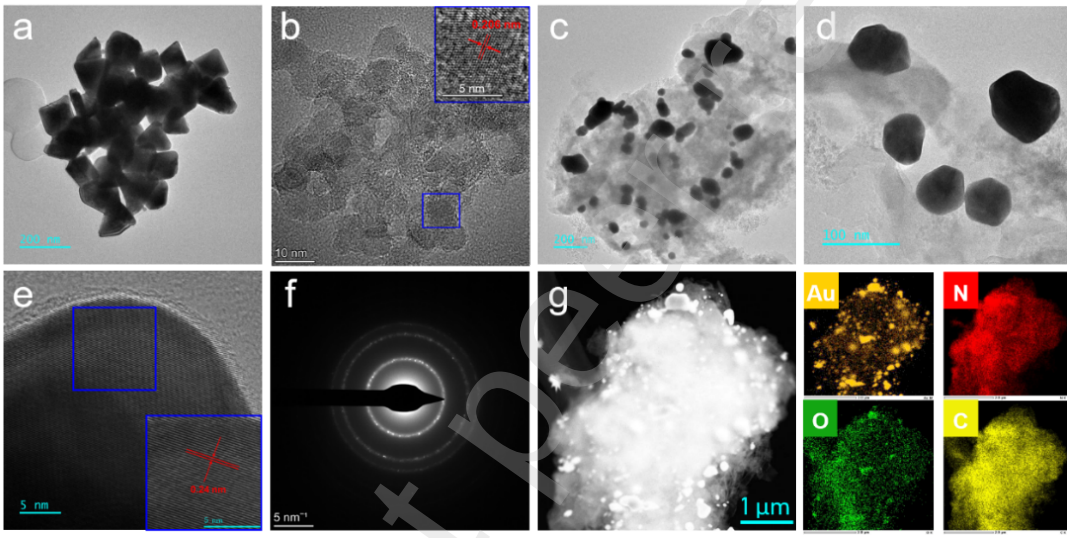

Figure 3. (a) TEM image of heterohedral Au NPs. (b) HRTEM image of ND/C_3N_4 hybrids. (c-e) TEM images of Au/ND/C_3N_4 hybrids at three different magnifications. (f) Selected area electron diffraction pattern of Au/ND/C_3N_4. (g) Elemental mapping images of Au/ND/C_3N_4.

Fig. 3c-e display the TEM images of Au/ND/C_3N_4 hybrid. As shown in Fig. 3c, Au NPs with a mean size of 96 nm are uniformly decorated on the surface and stacked layers of ND/C_3N_4, whereas, the particle size difference between Au NPs is large. At a higher magnification, abundant cavities can be observed on C_3N_4 nanosheets (Fig. S10). The produced cavities may enlarge adsorption capacity of the hybrid. Fig. 3d reveals that Au NPs in Au/ND/C_3N_4 hybrid retain heterohedral morphology with nanotips. And the nanotips display lattice fringes with an interplanar spacing of 0.24 nm, corresponding to the (111) facet of Au

NPs, as shown in Fig. 3e. Selected area electron diffraction pattern of Au/ND/C_3N_4 hybrid manifests three ring-shaped diffuse diffraction patterns, corresponding to the (111), (220) and (311) facets of ND, respectively (Fig. 3f). The diffraction ring also confirms the tight binding of ND and C_3N_4. The uniform distribution of Au, C, and N element in Fig. 3g indicates successful synthesis of Au/ND/C_3N_4 hybrid. The presence of O element may be assigned to oxygen-containing functional groups of ND and moisture adsorbed by the hybrid.

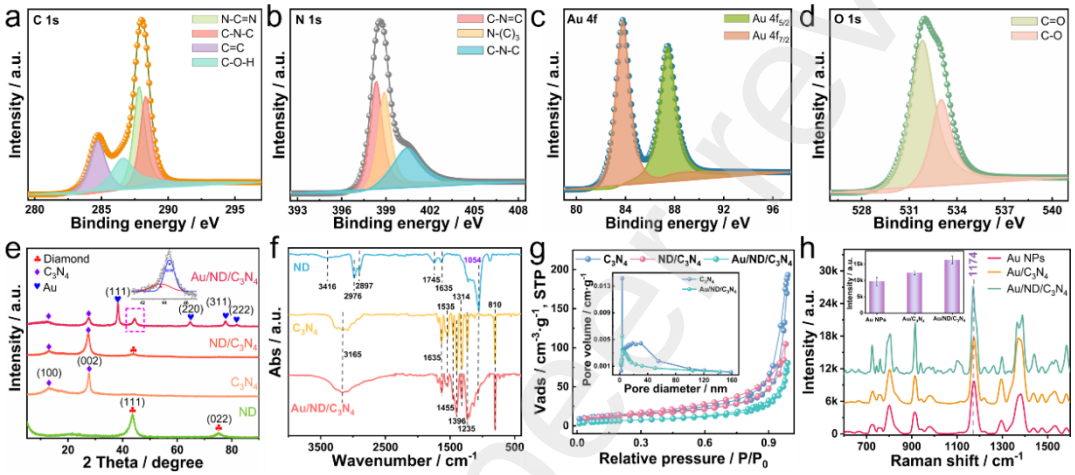

Figure 4. (a-d) XPS high-resolution spectra of the C 1s, N 1s, Au 4f and O 1s of Au/ND/C_3N_4 hybrid. (e) XRD patterns of ND, C_3N_4, ND/C_3N_4 and Au/ND/C_3N_4 hybrid. (f) FT-IR spectra of ND, C_3N_4 and Au/ND/C_3N_4 hybrid. (g) Nitrogen adsorption-desorption isotherms of C_3N_4, ND/C_3N_4 and Au/ND/C_3N_4, the insert is the pore size distribution profiles of C_3N_4 and Au/ND/C_3N_4. (h) SERS spectra of 10^{-4} M CV adsorbed onto the Au NPs, Au/C_3N_4 and Au/ND/C_3N_4 substrates accordingly.

XPS was employed to analyse chemical composition and surface chemical state of Au/ND/C_3N_4 hybrid. XPS survey spectrum reveals four distinct peaks corresponding to C 1s, N 1s, Au 4f and O 1s (Fig. S11), indicating successful synthesis of Au/ND/C_3N_4 hybrid. The high-resolution spectrum of the C 1s is shown in Fig. 4a. It can be deconvoluted into four characteristic bands located at 284.7, 286.6, 287.8, 288.3 and 286.6 eV, assigned to pure graphitic sites in the CN matrix (C=C), sp^2-C attached to NH_2 group in the aromatic ring (N-C=N), sp^2-C bonded to N in an aromatic ring (C-N-C) and sp^3-C of C-O-H group,

respectively [48, 49]. The emergence of sp^3-C concretely confirms successful residing of ND. Likewise, the high-resolution spectrum of N 1s can be deconvoluted into three bands of 398.3, 398.9 and 400.4 eV (Fig. 4b), corresponding to C-N=C, N-$(C)_3$, and C-N-C coordination accordingly [50]. In Fig. 4c, the spectrum of Au 4f comprises two peaks ascribed to Au $4f_{5/2}$ (83.7 eV) and Au $4f_{7/2}$ (87.4 eV) [51]. The high-resolution plot of O 1s could be curve-fitted with two bands due to C=O (531.8 eV) and C-O (533.0 eV) (Fig. 4d), revealing that ND addition introduces new functional groups into Au/ND/C_3N_4 hybrid [52].

XRD was used to characterize the phase structure of ND, C_3N_4, ND/C_3N_4 and Au/ND/C_3N_4, as shown in Fig. 4e. ND displays two sharp peaks at 2 theta of 43.9° and 75.3°, corresponding to the (111) and (220) facets of diamond, respectively [53]. Besides, a broad peak at 2 theta of 26° is attributed to the graphite phase on ND surface. This peak reveal that the purified ND powder consists of diamond and trace graphite [52]. C_3N_4 exhibits two peaks located at 13.1° and 27.6° assigned to (100) and (002) facets, respectively. The two peaks are sequentially assigned to in-plane structural packing motif of tri-s-triazine units and stacking of the conjugated aromatic system [54]. For ND/C_3N_4 hybrid, the characteristic peaks of C_3N_4 and ND are well preserved, indicating a favourable interaction of ND and C_3N_4. The absence of the (220) peak of ND may be due to the small amount of used ND. The XRD pattern of Au/ND/C_3N_4 hybrid features new peaks at 2 theta of 38.2°, 64.5°, 77.6° and 81.8°, corresponding to the (111), (220), (311) and (222) facets of Au NPs, respectively [29]. The peak at 44.1° can be deconvoluted into (111) facet (43.9°) of ND and (200) facet (44.3°) of Au NPs, as shown in inset of Fig. 4e.

Fig. S12 displays the Raman spectra of ND, C_3N_4, ND/C_3N_4 and Au/ND/C_3N_4. A sharp peak at 1332 cm^{-1} assigned to sp^3-C of diamond can be observed in the Raman spectrum of ND. The rough baseline is caused by strong fluorescence under laser excitation [55]. Moreover, no characteristic peak of sp^2-C is evident in the Raman spectrum. This may involve two aspects: (1) the

characteristic peak intensity of sp^2-C is weak due to its trace amount; (2) the peak is annihilated by the strong fluorescence. Four peaks are observed at 683, 775, 1215 and 1460 cm^{-1} in the case of C_3N_4, and are all ascribed to vibration modes of CN heterocycles [56]. For both ND/C_3N_4 and Au/ND/C_3N_4, the characteristic peaks of C_3N_4 are still obvious while the characteristic peak of ND is not seen. The difference lays in that the broad peak at 1317 cm^{-1} of C_3N_4 drifts to 1328 cm^{-1} after adding ND. The peak shift may be attributed to interaction of ND and C_3N_4, in good agreement with XPS data.

Furthermore, FT-IR spectra were acquired to analyse the surface functional groups of the prepared samples, as shown in Fig. 4f. It is apparent that ND surface embraces abundant functional groups, and these functional groups are favourably introduced into Au/ND/C_3N_4 hybrid. Characteristic peaks at 1054, 1635, 1745 and 3416 cm^{-1} of ND correspond to C−O stretching vibrations of epoxy groups, O−H deformation vibrations of COOH groups, C=O stretching vibrations of COOH groups and -OH stretching, respectively [57]. The two peaks at 2897 and 2976 cm^{-1} are assigned to C-H stretching vibration of saturated carbon [58]. In the FT-IR spectrum of C_3N_4, the characteristic peaks at 1235, 1314, 1396, 1455, 1535, and 1635 cm^{-1} are assigned to typical stretching modes of CN heterocycles. The peaks at 810 and 3144 cm^{-1} correspond to breathing mode of triazine units and stretching vibrations of -NH, respectively [59]. For Au/ND/C_3N_4 hybrid, the characteristic peaks of C_3N_4 remain clear and the peak at 1054 cm^{-1} of ND can still be observed, suggesting that synthesis process of Au/ND/C_3N_4 does not break the chemical structure of each component. Copious functional groups of Au/ND/C_3N_4 hybrid may strengthen its self-cleaning capability and promote analyte enrichment.

N_2 physical adsorption isotherm was utilized to discriminate surface area difference among C_3N_4, ND/C_3N_4 and Au/ND/C_3N_4. Fig. 4g depicts N_2 adsorption-desorption isotherms of C_3N_4, ND/C_3N_4 and Au/ND/C_3N_4. The surface area and pore volume of the prepared samples gradually decrease with loading ND and Au NPs in sequence. C_3N_4 features an IV-type isotherm with

H3-type hysteresis loop under high relative pressure, indicating the construction of copious mesopores with the help of Z204 catalyst [60]. Brunauer-Emmett-Teller (BET) surface area of C_3N_4 is 48.39 m^2 g^{-1}. S_{BET} of ND/C_3N_4 hybrid drops to 44.76 m^2 g^{-1}. The slight decrease of S_{BET} may be attributed to pore blocking caused by ND embedding in the cavities. S_{BET} of Au/ND/C_3N_4 hybrid sharply declined to 24.26 m^2 g^{-1}, suggesting that numerous Au NPs are embedded in C_3N_4 mesopores. Furthermore, Barrett-Joyner-Halenda (BJH) was applied to deduce pore size distribution (PSD) plots of C_3N_4 and Au/ND/C_3N_4, as shown in the inset of Fig. 4g. Pore volume of Au/ND/C_3N_4 is reduced to 0.125 cm^3 g^{-1}, as compared with its counterpart C_3N_4 (0.299 cm^3 g^{-1}). It is reasonable to speculate that Au NPs grow in C_3N_4 mesopores and are embedded in C_3N_4 nanosheets. The holey structure of C_3N_4 is favourable for anchoring Au NPs and inhibiting their agglomeration to improve the reproducibility of SERS signals.

To directly identify the effect of ND on SERS activity, SERS signal variation of CV probes on Au NPs, Au/C_3N_4 and Au/ND/C_3N_4 substrates were compared. Fig. 4h depicts the Raman spectra of 10^{-4} M CV adsorbed onto the three substrates. Pure Au NPs substrate has the lowest SERS activity, which may be due to its weak enrichment ability [61]. Au/C_3N_4 substrate exhibits an enhanced SERS activity. This can be attributed to two following facts: (1) the holey C_3N_4 ameliorates substrate enrichment capacity, (2) the heterostructure of Au NPs and C_3N_4 accelerates polarization of CV molecules [62]. Au/ND/C_3N_4 substrate acquires the strongest SERS signal, which provides the most direct evidence for SERS activity improvement upon ND addition. Moreover, the enhancement factor (EF) of the three substrates, which is calculated based on Fig. 4h and Fig. S13, confirms the same result. Au/ND/C_3N_4 substrate has the highest EF of 6.67×10^6, which is 2.01 and 1.58 times of that Au NPs (3.32×10^6) and Au/C_3N_4 (4.21×10^6) substrates, respectively.

3.2. SERS performance of self-cleaning Au/ND/C_3N_4 substrate

A systematic investigation was conducted on sensitivity, reproducibility and stability of the fabricated Au/ND/C_3N_4 substrate to assess its application prospect.

Substrate sensitivity was measured by SERS spectra of CV solutions with different concentrations, as shown in Fig. 5a, b. In Fig. 5a, the Raman intensity at 1174 cm^{-1} gradually drops upon decreasing CV solution concentration. Visible characteristic peaks can be observed even for a CV concentration of 10^{-14} M, indicating a high sensitivity of the substrate. Furthermore, logarithmic concentration and Raman intensity are linearly fitted to determine quantitative SERS detection, as shown in Fig. 5b. The logarithm concentration of CV maintains a good linear relationship with SERS intensity in a concentration range from 10^{-14} to 10^{-5} M. The calibration equation is: I_{SRES}=912 lgC_{CV}+12874, and the linear correlation coefficient (R^2) is 0.978. No SERS signals are recorded when CV concentration is lower than 10^{-14} M as only very few molecules lay at the laser spot area.

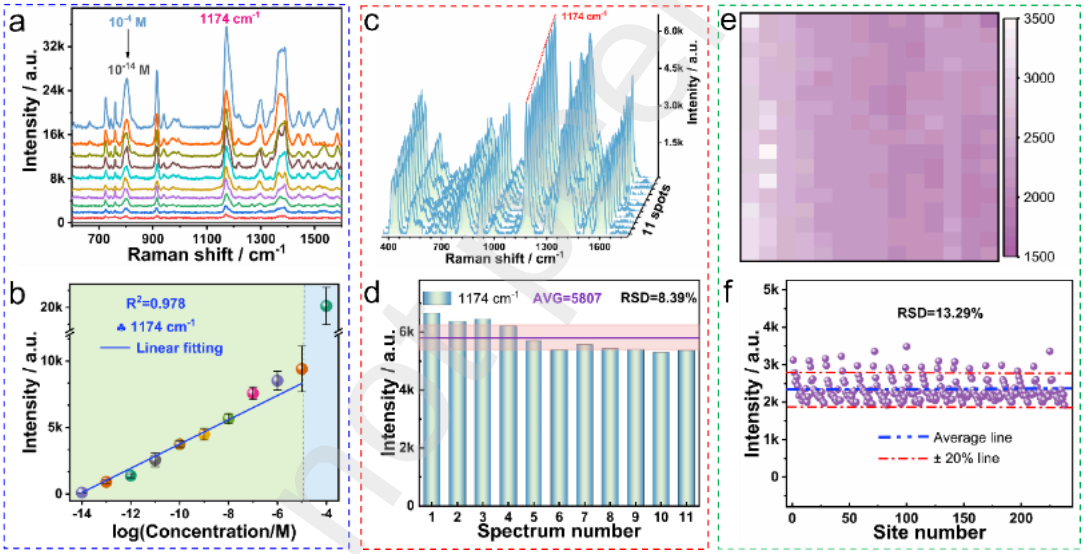

Figure 5. (a) SERS spectra of CV in a concentration range from 10^{-4} to 10^{-14} M recorded from Au/ND/C_3N_4 substrate. (b) Linear calibration plot of the SERS intensity at 1174 cm^{-1} versus logarithmic CV concentration. (c) SERS spectra of 10^{-8} M of CV obtained on random 11 spots from Au/ND/C_3N_4 substrate. (d) The corresponding histogram of intensity distribution of the 11 random spots at 1174 cm^{-1}. (e) SERS mappings (150×170 μm^2, step size of 10 μm) of the peak value at 1174 cm^{-1} recorded from Au/ND/C_3N_4 substrates exposed to 10^{-10} M CV solution. (f) Intensity distribution at 1174 cm^{-1} for all the 238 points in SERS mapping.

High reproducibility of SERS signals is another indispensable index for practical quantitative assay. Herein, reproducibility was determined by recording SERS signal variation of random substrate sites and calculating the relative standard deviation (RSD) value. Fig. 5c, d depicts SERS spectra of 10^{-8} M CV at 11 random points on Au/ND/C_3N_4 substrate and the intensity distribution histogram at 1174 cm^{-1}. RSD value of the 11 points is calculated to be 8.39%. Moreover, 238 random points in 150×170 μm^2 region were selected to conduct point-by-point measurement for verifying detection reliability of the SERS substrate using a 10^{-10} M CV solution. Fig. 5e reveals the mapping diagram of the peak intensity at 1174 cm^{-1}, where the SERS signal is uniformly distributed. RSD value of the 238 random points is 13.29% (Fig. 5f), suggesting an acceptable substrate reliability to generate reproducible SERS signals.

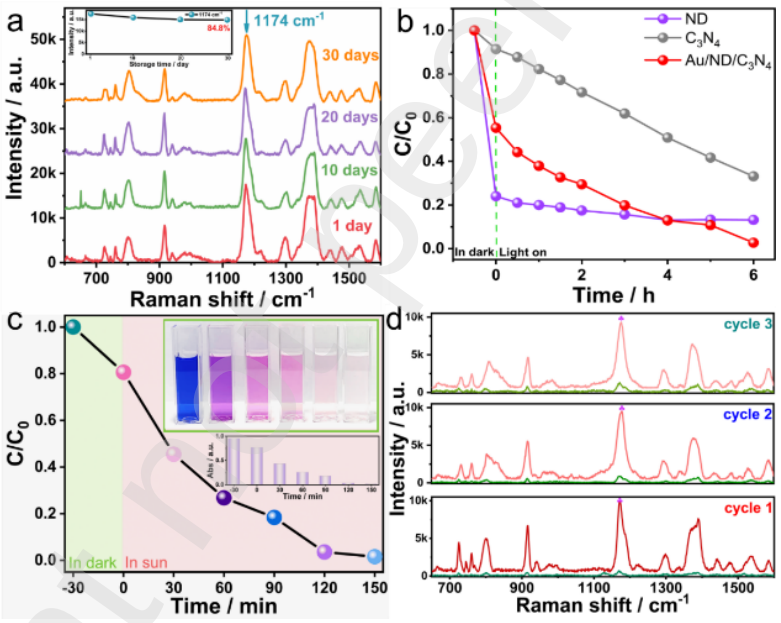

Figure 6. (a) SERS spectra of 10^{-4} M CV collected from Au/ND/C_3N_4 substrate with different storage times. (b) Photocatalytic degradation curves of 10^{-5} M CV in the presence of ND, C_3N_4 and Au/ND/C_3N_4 hybrid. (c) Photocatalytic degradation curves of 10^{-5} M CV in the presence of Au/ND/C_3N_4 hybrid (under sunlight illumination from 12:00 to 14:30). (d) Self-cleaning test of Au/ND/C_3N_4 substrate through three cycles of SERS detection and photocatalytic degradation of 10^{-5} M CV.

Furthermore, stability was assessed by SERS signal variation of CV on Au/ND/C_3N_4 substrates with different storage times. The storage condition was air

environment, and the concentration of CV solution was 10^{-4} M. Fig. 6a depicts SERS spectra of CV on Au/ND/C_3N_4 substrates with 1-, 10-, 20- and 30-days storage. The signal retention is 84.8% after 30 days, indicating a superior environmental stability. Such stability may be attributed to two aspects: (1) good chemical stability of Au NPs; (2) charge transfer between Au NPs and ND/C_3N_4 hybrid [63].

Apart from admirable SERS performance, the self-cleaning capability of Au/ND/C_3N_4 is an essential factor for its actual application. To investigate this capability, photocatalytic activities of Au/ND/C_3N_4 hybrid, as well as ND and C_3N_4 were assessed for the decomposition of CV under visible light irradiation. The degradation rates were determined by recording the change of UV-vis spectra at 590 nm. And C/C_0 was calculated to mirror the degradation rate value, wherein, C_0 and C were the initial absorbance and absorbance at a certain reaction time, respectively. Fig. 6b depicts the degradation curves of CV solution in presence of the above three samples. Au/ND/C_3N_4 hybrid exhibits the best photocatalytic activity, and its degradation rate is 97.3% after 6 h visible light irradiation. Degradation rate of Au/ND/C_3N_4 is nearly 1.5 times higher than that of pure C_3N_4 (degradation rate=66.8%). This enhanced photocatalytic activity is mainly ascribed to the formation of a heterojunction, which improves the charge separation efficiency [64]. Specifically, photogenerated electrons excited by C_3N_4 under irradiation will transfer to ND due to the more negative conduction band of C_3N_4 than ND [46]. Au NPs may also take over the electrons from C_3N_4 since its outstanding electron conduction feature [65]. And the LSPR effect of Au NPs is another avenue to excite electrons [66]. Those electrons produce free radical species for decomposing CV molecules. Subsequently, the photodegradation performance of Au/AND/C_3N_4 hybrid is evaluated under sunlight, as shown in Fig. 6c. The results reveal that CV can be degraded almost completely (96.4%) by Au/ND/C_3N_4 hybrid within 150 min. Such photocatalytic activity directly confirms the good self-cleaning ability of Au/ND/C_3N_4.

To have a better understanding of self-cleaning features of Au/ND/C_3N_4 substrate, a systematic investigation was conducted on SERS detection and photodegradation of CV for three cycles. Each cycle comprises three steps: (1) the CV solution was mixed

with Au/ND/C_3N_4 hybrid for enrichment; (2) SERS detection was executed and the hybrid was recovered to implement CV photocatalytic degradation after SERS measurement; (3) the recovered Au/ND/C_3N_4 hybrid was cleaned and dried for the next cycle. As shown in Fig. 6d, retention rate of SERS intensity at 1174 cm^{-1} is 92.1% after three cycles, indicating an acceptable attenuation of SERS detection capability. The SERS signal of remaining CV molecules gradually raises with increasing the number of photodegradation cycles. This may be due to the accumulation of residues, as well as reduction of photocatalytic activity. In brief, fingerprint signal intensity has a small difference among the three cycles, revealing a good self-cleaning feature of Au/ND/C_3N_4 substrate and a broad prospect for recyclable detection.

3.3. Application of self-cleaning Au/ND/C_3N_4 substrate for tetracycline detection

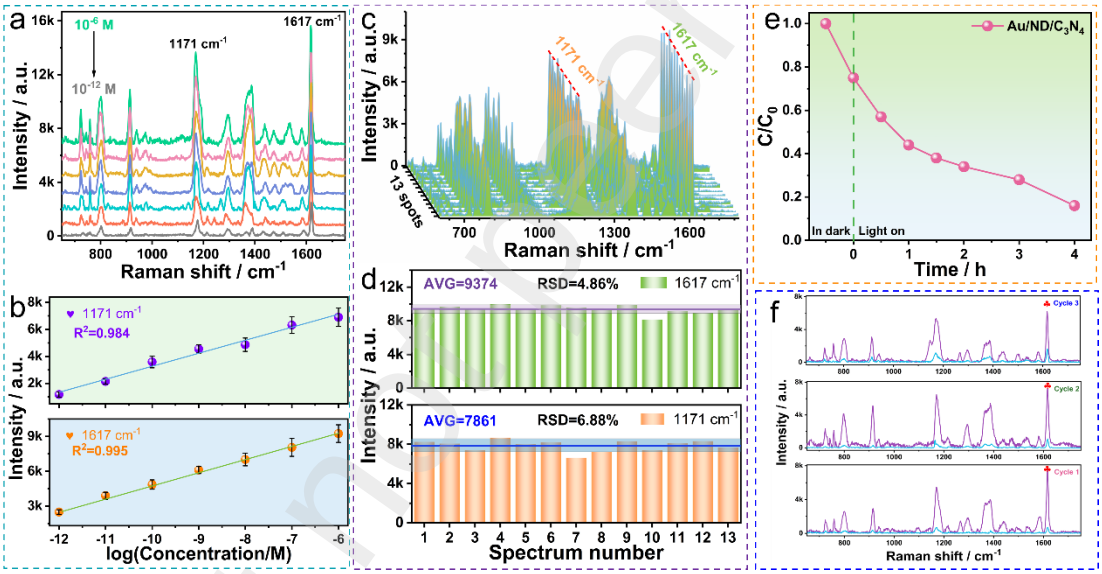

Figure 7. (a) SERS spectra of tetracycline in a concentration range from 10^{-6} to 10^{-12} M recorded using Au/ND/C_3N_4 substrate. (b) Linear calibration plots of the SERS intensities at 1171 and 1617 cm^{-1} versus logarithmic of tetracycline concentration. (c) SERS spectra of a 10^{-6} M tetracycline solution recorded on random 13 spots using Au/ND/C_3N_4 substrate. (d) The corresponding histogram of intensity distribution of the 13 random spots at 1171 and 1617 cm^{-1}. (e) Photocatalytic degradation curves of a 10^{-5} M tetracycline in the presence of Au/ND/C_3N_4 hybrid (under visible-light illumination). (f) Self-cleaning test of Au/ND/C_3N_4 substrate through three cycles of SERS detection and photocatalytic degradation of 10^{-7} M tetracycline.

In view of the superior performance achieved by Au/ND/C_3N_4 substrate, it is further adopted for tetracycline detection. To begin with, the detection sensitivity of Au/ND/C_3N_4 substrate for tetracycline was assessed. Fig. 7a depicts the SERS spectra of tetracycline in a concentration range from 10^{-6} to 10^{-12} M on Au/ND/C_3N_4 substrate. The attributions of selected peaks (1171 and 1617 cm^{-1}) for tetracycline are listed in Table S1, as well as those of other possible characteristic peaks. Visible selected peaks can be observed even for a tetracycline concentration of 10^{-12} M, indicating a high sensitivity of Au/ND/C_3N_4 substrate. The linear fitting plot of logarithmic concentration and SERS intensity is shown in Fig. 7b. In a concentration range from 10^{-6} to 10^{-12} M, the calibration equation for 1171 cm^{-1} peak is: $\boldsymbol{I_{SRES}}$=1015 $\boldsymbol{logC_{Tetracycline}}$ +13388, and the R^2 is 0.984. The calibration equation for the 1617 cm^{-1} peak is: $\boldsymbol{I_{SRES}}$=1143 $\boldsymbol{logC_{Tetracycline}}$+16281, with R^2=0.995. The superior sensitivity of Au/ND/C_3N_4 substrate is also been certificated by the performance comparison for TC detection with other SERS substrates, as listed in Table S2. Subsequently, SERS reproducibility of Au/ND/C_3N_4 substrate was determined. Fig. 7c, d display SERS spectra of 10^{-6} M tetracycline solution at 13 random points on Au/ND/C_3N_4 substrate, and the histogram of peak intensity distributions at 1171 and 1617 cm^{-1}. The RSD values of peak intensities at 1171 and 1617 cm^{-1} are respectively 4.86% and 6.88%, proving high SERS signal reproducibility of the substrate.

Likewise, the self-cleaning property of Au/ND/C_3N_4 hybrid was evaluated for the decomposition of tetracycline solution under visible light irradiation, as shown in Fig. 7e. The degradation rate of tetracycline is 86.1% after 4 h irradiation in presence of Au/ND/C_3N_4, repeatedly confirming its good self-cleaning capability. Furthermore, a systematic investigation was conducted on SERS detection and photodegradation of tetracycline under three cycles. As shown in Fig. 7f, the retention rate of SERS intensity at 1617 cm^{-1} is 87.1% after three cycles. The small difference of signal intensities suggests that Au/ND/C_3N_4 substrate is suitable for self-cleaning detection of tetracycline.

3.4. Possible mechanism

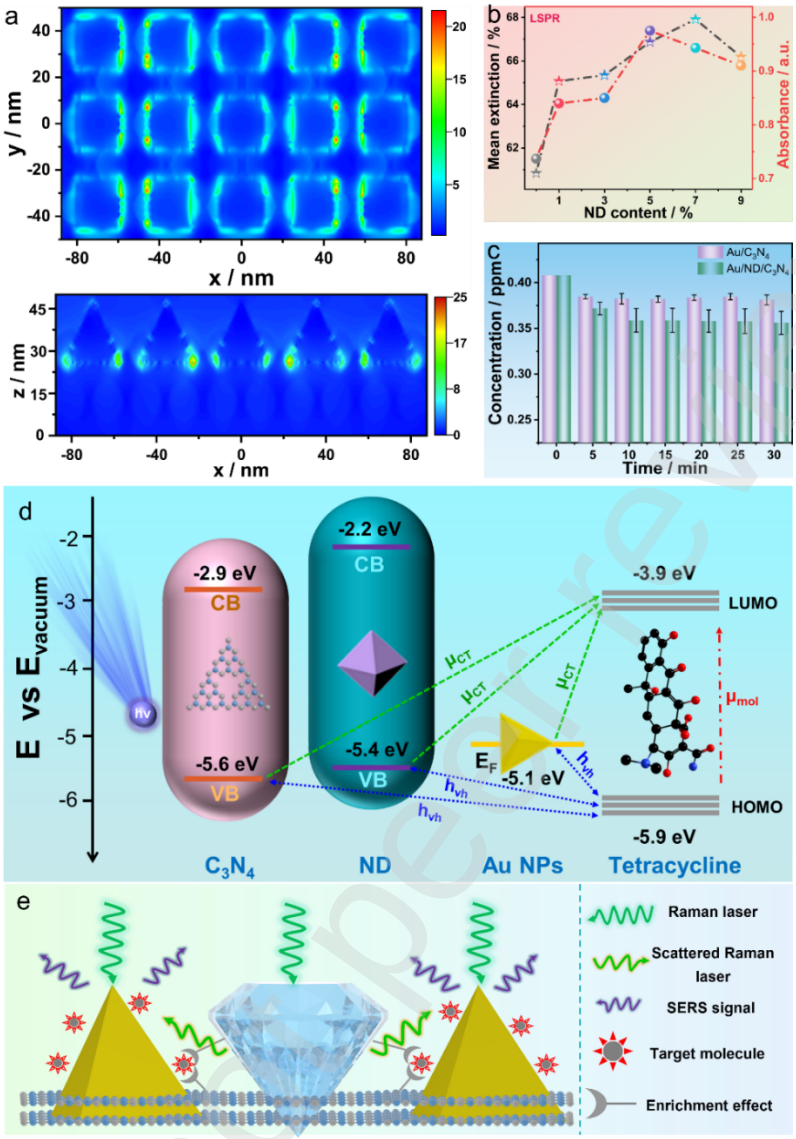

Figure 8. (a) Contour plots of the electric field distribution of Au/ND/C_3N_4 substrate simulated by FDTD. (b) Optical properties variation of Au NPs in Au/ND/C_3N_4 hybrids upon ND content. (c) The concentration variation of CV solution with adsorption time in the presence of Au/C_3N_4 (10 mg) and Au/ND/C_3N_4 (10 mg) hybrids, respectively. (d) Energy-level diagram and possible CT paths between Au/ND/C_3N_4 substrate and target molecule. (e) Schematic mechanism of Au/ND/C_3N_4 substrate for the enhanced SERS activity in the presence of ND.

To better understand the enhancement effect of ND on SERS signal, electric field distribution of Au/ND/C_3N_4 substrate under 633 nm laser was simulated by FDTD, as shown in Fig. 8a. The FDTD result of x-y view mirrors the electric field distribution for coupling region of Au NPs and ND, while x-z view may mirror the electric field

distribution for non-coupling region. The coupling region behaves a stronger field enhancement than that of non-coupling region. This phenomenon is ascribed to the high light utilization brought by ND. On the other hand, the supporting video shows the electric field variation over time of the two views, and the non-coupling region features a delayed field enhancement than coupling region. This delayed electric field enhancement may be attributed to scattering effect of ND for the Raman laser beam. The scattered laser beam irradiates Au NPs again to generate a sub-enhanced electric field. Those results prove well that ND scattering may assist enhancement of electric field and bring EM enhancement. In addition, the edges and tips of Au NPs have the highest electric field strength due to LSPR effect, suggesting that the heterohedral morphology of Au NPs could offer sufficient EM enhancement for analyte.

Fig. 8b depicts the optical properties variation of Au NPs in Au/ND/C_3N_4 hybrids with ND content. Obviously, the introduction of ND efficiently strengthens the LSPR effect of Au NPs. The maximum extinction ratio and maximum absorbance of Au NPs are increased by 1.12 times and 1.32 times, respectively. Combined with Fig. 2g and Fig. S3, it is reasonable to speculate that the light scattering properties of ND effectively enhance light utilization of Au/ND/C_3N_4 substrate, thus offering a stronger EM enhancement. This phenomenon may be ascribed to the high optical refractive index of ND (2.42) [46]. Furthermore, concentration variation of CV solution over time was recorded using Au/C_3N_4 and Au/ND/C_3N_4 hybrids to investigate the influence of ND on enrichment capacity, as shown in Fig. 8c. The CV concentration reaches equilibrium after 10 min for both ND/C_3N_4 and Au/ND/C_3N_4 hybrids, but the CV solution in presence of Au/ND/C_3N_4 exhibits a lower residual concentration than that of Au/C_3N_4. This indicates that Au/ND/C_3N_4 substrate has a stronger enrichment capability and may capture more analyte molecules for producing SERS signals. Such superior enrichment capability of Au/ND/C_3N_4 substrate is attributed to a synergistic effect of ND functional groups and the holey C_3N_4 structure on analyte adsorption.

Subsequently, possible polarization paths of analyte molecules are analysed from the perspective of energy levels. Fig. 8d displays energy level diagram of charge transfer between Au/ND/C_3N_4 substrate and target molecules. The Fermi level (E_F) of

AuNPs is located at -5.1 eV; the valence bands of ND and C_3N_4 are located at -5.4 and -5.6 eV, and conduction bands are at -2.2 and -2.9 eV, respectively [46, 67]. The highest occupied molecular orbital (HOMO) and the lowest unoccupied molecular orbital (LUMO) levels of tetracycline are located at -5.9 and -3.9 eV, respectively [68]. Under laser radiation, the energy provided by excitation wavelength at 633 nm (1.95 eV) is not enough to trigger the intramolecular electronic transition between HOMO and LUMO of tetracycline. Instead, energy difference between each component of Au/ND/C_3N_4 and HOMO of tetracycline matches well with the energy of Raman photons. Hence, Au/ND/C_3N_4 may act as a charge transfer medium to push photon-induced CT (μ_{CT}) processes, as illustrated in Fig. 8d. The μ_{CT} with multi-channels could enlarge Raman scattering cross-section to enhance SERS signal. Meanwhile, the excited photothermal electrons of Au NPs may also transfer to LUMO level of tetracycline and induce molecular polarization [67].

The above data allow us to propose a ND improvement mechanism for SERS activity, as illustrated in Fig. 8e. The proposed mechanism involves four aspects: (1) **EM effect of heterohedral Au NPs.** Due to LSPR effect, heterohedral Au NPs exhibit a strong electromagnetic field distribution at edges with small curvature radiuses such as nano-tips, and will excite SERS signals. (2) **Enrichment effect.** Abundant functional groups on ND may effectively capture analyte molecules and favour the enrichment of molecules on SERS substrate. More target molecules are enriched on the substrate and receive Raman irradiation, resulting in a stronger SERS signal. In addition, the holey morphology of C_3N_4 and optical plasmons of Au NPs also contribute to the enrichment effect [69]. (3) **CT effect of Au/ND/C_3N_4 heterostructure**. With the help of energy ladder from Au/ND/C_3N_4 heterostructure, analyte molecules may readily undergo a charge transfer from HOMO to LUMO under excitation of Raman photons. Charge transfer process induces polarization of analyte molecules, resulting in SERS enhancement. (4) **Sub-enhancement from light scattering of ND**. ND can scatter Raman laser due to its high refractive index. In coupling region of Au NPs and ND, the laser beam and scattered light jointly excite Au NPs to generate SERS hot spots by means of high light utilization. In non-coupling region, the scattered light excites Au

NPs again to contribute an enhanced electric field with a sub-intensity, and offers a SERS signal. More commendably, the enhanced electric field in non-coupling region may boost long-range SERS detection to overcome the poor affinity of Au NPs, thus acquiring high sensitivity [70]. Here, we label those SERS enhancements from the scattered Raman laser as sub-enhancement.

4. Conclusions

In conclusion, Au/ND/C_3N_4 SERS substrate of featuring light-enhancement and self-cleaning properties was successfully constructed by the combination of ND, C_3N_4 and Au NPs. The abundant functional groups and light scattering effect of ND endowed Au/ND/C_3N_4 substrate with excellent enrichment capability and sub-enhancement of SERS signal. Thus, the prepared substrate exhibited a favourable SERS activity and allowed highly sensitive detection of CV and tetracycline at low concentrations of 10^{-14} M and 10^{-12} M, respectively. In addition, the hybrid exhibited high catalytic activity due to the enhanced electron separation efficiency, and featured a self-cleaning behaviour. The satisfactory reproducibility and stability of this substrate confirmed its good potential in actual analysis application. Adopting light scattering effect to improve SERS activity provides a good avenue for the fabrication of high-performance SERS substrates. Meanwhile, all the superior performances may allow Au/ND/C_3N_4 hybrids to be applied for sensitive assays of antibiotic residues in wastewater.

Declaration of Competing Interest

The authors declare that they have no known competing financial interests or personal relationships that could have appeared to influence the work reported in this paper.

Acknowledgements

This work was supported by the National Natural Science Foundation of China [grant number 51571183] and the 2021 Graduate Innovation Fund Project of China University of Geosciences, Beijing [grant number ZY2021YC002]. The authors would like to thank Shuai Zhang from Shiyanjia Lab (www.shiyanjia.com) for the FDTD simulation.

References

[1] X.R. Yang, Z. Chen, W. Zhao, C.X. Liu, X.X. Qian, M. Zhang, G.Y. Wei, E. Khan, Y.H. Ng, Y.S. Ok, Recent advances in photodegradation of antibiotic residues in water, Chem. Eng. J. 405 (2021) 126806.

[2] Q.T. Dinh, E. Moreau-Guigon, P. Labadie, F. Alliot, M.J. Teil, M. Blanchard, M. Chevreuil, Occurrence of antibiotics in rural catchments, Chemosphere 168 (2017) 483-490.

[3] P. Chaturvedi, P. Shukla, B.S. Giri, P. Chowdhary, R. Chandra, P. Gupta, A. Pandey, Prevalence and hazardous impact of pharmaceutical and personal care products and antibiotics in environment: A review on emerging contaminants, Environ. Res. 194 (2021) 110664.

[4] E.Y. Klein, M. Milkowska-Shibata, K.K. Tseng, M. Sharland, S. Gandra, C. Pulcini, R. Laxminarayan, Assessment of WHO antibiotic consumption and access targets in 76 countries, 2000-15: An analysis of pharmaceutical sales data, Lancet Infect. Dis. 21(1) (2021) 107-115.

[5] P. Chaturvedi, A. Singh, P. Chowdhary, A. Pandey, P. Gupta, Occurrence of emerging sulfonamide resistance (sul1 and sul2) associated with mobile integrons-integrase (intI1 and intI2) in riverine systems, Sci. Total Environ. 751 (2021) 142217.

[6] P. Chaturvedi, D. Chaurasia, A. Pandey, P. Gupta, Co-occurrence of multidrug resistance, beta-lactamase and plasmid mediated AmpC genes in bacteria isolated from river Ganga, northern India, Environ. Pollut. 267 (2021) 115502.

[7] M.E.A. de Kraker, A.J. Stewardson, S. Harbarth, Will 10 million people die a year due to antimicrobial resistance by 2050? PLoS Med. 13(11) (2016) 1-6.

[8] M. Ramezani, N.M. Danesh, P. Lavaee, K. Abnous, S.M. Taghdisi, A novel colorimetric triple-helix molecular switch aptasensor for ultrasensitive detection of tetracycline, Biosens. Bioelectron. 70 (2015) 181-187.

[9] M.R. Chao, C.W. Hu, J.L. Chen, Comparative syntheses of tetracycline-imprinted polymeric silicate and acrylate on CdTe quantum dots as fluorescent sensors, Biosens. Bioelectron. 61 (2014) 471-477.

675 [10] W.S. Zeng, C.Y. Zhu, H.C. Liu, J. Liu, H.P. Cai, X.L. Cheng, L.J. Wei,
676 Ultrasensitive chemiluminescence of tetracyclines in the presence of MCLA, J.
677 Lumin. 186 (2017) 158-163.
678 [11] S. Jahanbani, A. Benvidi, Biosens. Bioelectron. Comparison of two fabricated
679 aptasensors based on modified carbon paste/oleic acid and magnetic bar carbon
680 paste/Fe_3O_4@oleic acid nanoparticle electrodes for tetracycline detection, Biosens.
681 Bioelectron. 85 (2016) 553-562.
682 [12] L.P. Zong, J.J. Li, G.F. Shu, X.Y. Liu, R.S. Marks, X.J. Zhang, S. Cosnier, D. Shan,
683 Rational Design of a Highly Dispersed Fe-N-C Nanosheet with 1,10-
684 Phenanthroline-2,9-Dicarboxylic Acid as a Preorganized Ligand: Boosted
685 Electrochemiluminescence Detection of Tetracycline, Anal. Chem. 94(2) (2022)
686 1325-1332.
687 [13] X.G. Liu, D.L. Huang, C. Lai, G.M. Zeng, L. Qin, C. Zhang, H. Yi, B.S. Li, R.
688 Deng, S.Y. Liu, Y.J. Zhang, Recent advances in sensors for tetracycline antibiotics
689 and their applications, Trac-Trend. Anal. Chem. 109 (2018) 260-274.
690 [14] S.H. Jalalian, N. Karimabadi, M. Ramezani, K. Abnous, S.M. Taghdisi,
691 Electrochemical and optical aptamer-based sensors for detection of tetracyclines,
692 Trac-Trend. Anal. Chem. 73 (2018) 45-57.
693 [15] H.Z. Li, Q. Yang, J. Hou, Y.A. Li, M.Z. Li, Y.L. Song, Bioinspired micropatterned
694 superhydrophilic Au-areoles for surface-enhanced Raman scattering (SERS) trace
695 detection, Adv. Funct. Mater. 28(21) (2018) 1800448.
696 [16] B.W. Liu, X. Yao, S. Chen, H.X. Lin, Z.L. Yang, S. Liu, B. Ren, Large-area hybrid
697 plasmonic optical cavity (HPOC) substrates for surface-enhanced Raman
698 spectroscopy, Adv. Funct. Mater. 28(43) (2018) 1802263.
699 [17] Z.X. Lao, Y.Y. Zheng, Y.C. Dai, Y.L. Hu, J.C. Ni, S.Y. Ji, Z. Cai, Z.J. Smith, J.W.
700 Li, L. Zhang, D. Wu, J.R. Chu, Nanogap plasmonic structures fabricated by
701 switchable capillary-force driven self-assembly for localized sensing of anticancer
702 medicines with microfluidic SERS, Adv. Funct. Mater. 30(15) (2020) 1909467.
703 [18] X.Y. Zhang, Y.H. Zheng, X. Liu, W. Lu, J.Y. Dai, D.Y. Lei, D.R. MacFarlane,
704 Hierarchical porous plasmonic metamaterials for reproducible ultrasensitive

surface-enhanced Raman spectroscopy, Adv. Mater. 27(6) (2015) 1090-1096.

[19] S.Y. Ding, J. Yi, J.F. Li, B. Ren, D.Y. Wu, R. Panneerselvam, Z.Q. Tian, Nanostructure-based plasmon-enhanced Raman spectroscopy for surface analysis of materials, Nat. Rev. Mater. 1(6) (2016) 16021.

[20] N. Filippin, J. Castillo-Seoane, M.C. Lopez-Santos, C.T. Rojas, K. Ostrikov, A. Barranco, J.R. Sanchez-Valencia, A. Borras, Plasma-enabled amorphous TiO_2 nanotubes as hydrophobic support for molecular sensing by SERS, ACS Appl. Mater. Interfaces 12(45) (2020) 50721-50733.

[21] J.J. Li, H. Yan, X.C. Tan, Z.C. Lu, H.Y. Han, Cauliflower-inspired 3D SERS substrate for multiple mycotoxins detection, Anal. Chem. 91(6) (2019) 3885-3892.

[22] E. Bailo, V. Deckert, Tip-enhanced Raman scattering, Chem. Soc. Rev. 37(5) (2008) 921-930.

[23] J. Ye, F. Wen, H. Sobhani, J.B. Lassiter, P.V. Dorpe, P. Nordlander, N.J. Halas, Plasmonic nanoclusters: Near field properties of the Fano resonance interrogated with SERS, Nano Lett. 12(3) (2012) 1660-1667.

[24] A. Lahiri, R. Wen, S. Kuimalee, S. Kobayashi, H. Park, One-step growth of needle and dendritic gold nanostructures on silicon for surface enhanced Raman scattering, Crystengcomm, 14(4) (2012) 1241-1246.

[25] S. Park, J. Lee, H. Ko, Transparent and flexible surface enhanced Raman scattering (SERS) sensors based on gold nanostar arrays embedded in silicon rubber film, ACS Appl. Mater. Interfaces 9(50) (2017) 44088-44095.

[26] S.A. Razek, A.B. Ayoub, M.A. Swillam, One step fabrication of highly absorptive and surface enhanced Raman scattering (SERS) silver nano-trees on silicon substrate, Sci. Rep. 9 (2019) 13588.

[27] P.K. Kannan, P. Shankar, C. Blackman, C.H. Chung, Recent advances in 2D inorganic nanomaterials for SERS sensing, Adv. Mater. 31(34) (2019) 1803432.

[28] L.L. Qu, Z.Q. Geng, W. Wang, K.C. Yang, W.P. Wang, C.Q. Han, G.H. Yang, R. Vajtai, D.W. Li, P.M. Ajayan, Recyclable three-dimensional Ag nanorod arrays decorated with O-g-C_3N_4 for highly sensitive SERS sensing of organic pollutants, J. Hazard. Mater. 379 (2019) 120823.

[29] Y.N. Wang, Y. Zhang, W.S. Zhang, Z.R. Xu, A SERS substrate of mesoporous g-C_3N_4 embedded with in situ grown gold nanoparticles for sensitive detection of 6-thioguanine, Sensor. Actuat. B: Chem. 260 (2018) 400-407.

[30] J.Z. Jiang, J. Zou, A.T.S. Wee, W.J. Zhang, Use of single-layer g-C_3N_4/Ag hybrids for surface-enhanced Raman scattering (SERS), Sci. Rep. 6 (2016) 34599.

[31] X. Jin, Q.Y. Zhu, L. Feng, X. Li, H.Y. Zhu, H.Y. Miao, Z.F. Zeng, Y.D. Wang, Y. Li, L.K. Wang, X.F. Liu, G. Shi, Light-trapping SERS substrate with regular bioinspired arrays for detecting trace dyes, ACS Appl. Mater. Interfaces 13(9) (2021) 11535-11542.

[32] X.X. Li, Y. Shang, J. Lin, A.R. Li, X.T. Wang, B. Li, L. Guo, Temperature-induced stacking to create Cu_2O concave sphere for light trapping capable of ultrasensitive single-particle surface-enhanced Raman scattering, Adv. Funct. Mater. 28(33) (2018) 1801868.

[33] W.W. Li, L. Xiong, N.C. Li, S. Pang, G.L. Xu, C.H. Yi, Z.X. Wang, G.Q. Gu, K.W. Li, W.M. Li, L. Wei, G.Y. Li, C.L. Yang, Tunable 3D light trapping architectures based on self-assembled $SnSe_2$ nanoplate arrays for ultrasensitive SERS detection, J. Mater. Chem. C 7(33) (2019) 10179-10186.

[34] Y. Zeng, R.X. Gao, J.Y. Wang, T.M. Shih, G.Y. Sun, J.S. Lin, Y.L. He, J.W. Chen, D. Zhan, J.F. Zhu, W.M. Yang, P.W. Ren, F.F. Jiao, Z.L. Yang, Light-trapped nanocavities for ultraviolet surface-enhanced Raman scattering, J. Mater. Chem. C 125(31) (2021) 17241-17247.

[35] C. Li, S. Xu, J. Yu, S. Jiang, A. Liu, Z. Li, S. Zhang, X. Zhao, C. Zhang, B. Man, 3D hybrid MoS_2/AgNPs/inverted pyramid PMMA resonant cavity system for the excellent flexible surface enhanced Raman scattering sensor, Sensor. Actuat. B: Chem. 274 (2018) 152-162.

[36] J. Xu, C. Li, H. Si, X. Zhao, L. Wang, S. Jiang, D. Wei, J. Yu, X. Xiu, C. Zhang, 3D SERS substrate based on Au-Ag Bi-metal nanoparticles/MoS_2 hybrid with pyramid structure, Opt. Express 26(17) (2018) 21546-21557.

[37] Y. Li, L. Feng, J. Li, X. Li, J. Chen, L. Wang, D. Qi, X. Liu, G. Shi, Fabrication of an insect-like compound-eye SERS substrate with 3D Ag nano-bowls and its

765 application in optical sensor, Sensor. Actuat. B: Chem. 330 (2021) 129357.
766 [38] G.S. Li, Z.P. Xie, S.M. Chai, X. Chen, X.C. Wang, A facile one-step fabrication
767 of holey carbon nitride nanosheets for visible-light-driven hydrogen evolution,
768 Appl. Catal. B 283 (2021) 119637.
769 [39] V.N. Mochalin, O. Shenderova, D. Ho, Y. Gogotsi, The properties and applications
770 of nanodiamonds, Nat. Nanotechnol. 7(1) (2012) 11-23.
771 [40] M. Reddeppa, S.B. Mitta, T. Chandrakalavathi, B.G. Park, G. Murali, R.
772 Jeyalakshmi, S.G. Kim, S.H. Park, M.D. Kim, Solution-processed Au@rGO/GaN
773 nanorods hybrid-structure for self-powered UV, visible photodetector and CO gas
774 sensors, Curr. Appl. Phys. 19(8) (2019) 938-945.
775 [41] K.N. Kanipe, P.P.F. Chidester, G.D. Stucky, C.D. Meinhart, M. Moskovits,
776 Properly structured, any metal can produce intense surface enhanced Raman spectra,
777 J. Phys. Chem. C. 121(26) (2017) 14269-14273
778 [42] S. Pandit, S. Kunwar, R. Kulkarni, R. Mandavka, S. Lin, J. Lee, Fabrication of
779 hybrid Pd@Ag core-shell and fully alloyed bi-metallic AgPd NPs and SERS
780 enhancement of Rhodamine 6G by a unique mixture approach with graphene
781 quantum dots, Appl. Surf. Sci. 548 (2021) 149252.
782 [43] D. Sajan, G.D. Sockalingum, M. Manfait, I. Hubert Joe, V.S. Jayakumar, NIR-FT
783 Raman, FT-IR and surface-enhanced Raman scattering spectra, with theoretical
784 simulations on chloramphenicol, J. Raman Spectrosc. 39(12) (2008) 1772-1783.
785 [44] Y. Gao, T. You, N. Yang, C. Zhang, P. Yin, Superhydrophobic 3D forest-like Ag
786 microball/nanodendrite hierarchical structure as SERS sensor for rapid droplets
787 detection, Adv. Mater. Interfaces 6(8) (2019) 1801966.
788 [45] J.Y. Qu, J.F. Mukerabigwi, N.S. Yang, X.Y. Huang, Y.Y. Sun, X.J. Cai, Y. Cao,
789 Rapid separation of nanodiamond particles by viscosity gradient centrifugation,
790 Appl. Nanosci. 11(1) (2021) 257-266.
791 [46] L.X. Su, Q.Z. Huang, Q. Lou, Z.Y. Liu, J.L. Sun, Z.T. Zhang, S.R. Qin, X. Li, J.H.
792 Zang, L. Dong, C.X. Shan, Effective light scattering and charge separation in
793 nanodiamond@g-C_3N_4 for enhanced visible-light hydrogen evolution, Carbon 139
794 (2018) 164-171.

795 [47] L.X. Su, Q. Lou, J. Zhen, C.X. Shan, Plant cell imaging based on nanodiamonds
796 with excitation-dependent fluorescence, Nanoscale Res. Lett. 11 (2016) 425.
797 [48] J.J. Xue, S.S. Ma, Y.M. Zhou, Z.W. Zhang, M. He, Facile photochemical synthesis
798 of Au/Pt/g-C_3N_4 with plasmon-enhanced photocatalytic activity for antibiotic
799 degradation, ACS Appl. Mater. Interfaces 7(18) (2015) 9630-9637.
800 [49] L. Ge, C.C. Han, Synthesis of MWNTs/g-C_3N_4 composite photocatalysts with
801 efficient visible light photocatalytic hydrogen evolution activity, Appl. Catal. B 117
802 (2012) 268-274.
803 [50] J.P. Wang, J.K. Cong, H. Xu, J.M. Wang, H. Liu, M. M. Liang, J.K. Gao, Q.Q. Ni,
804 J.M. Yao, Facile gel-based morphological control of Ag/g-C_3N_4 porous nanofibers
805 for photocatalytic hydrogen generation, ACS Sustainable Chem. Eng. 5(11) (2017)
806 10633-10639.
807 [51] P. Wang, Z.G. Liu, X. Chen, F.L. Meng, J.H. Liu, X.J. Huang, UV irradiation
808 synthesis of an Au-graphene nanocomposite with enhanced electrochemical sensing
809 properties, J. Mater. Chem. A 1(32) (2013) 9189-9195.
810 [52] D, Lee, S. H. Jeong, E. Kang, Nanodiamond/gold nanorod nanocomposites with
811 tunable light-absorptive and local plasmonic properties, J. Ind. Eng. Chem. 65
812 (2018) 205-212.
813 [53] Z. Said, L.S. Sundar, H. Rezk, A.M. Nassef, S. Chakraborty, C.H. Li,
814 Thermophysical properties using ND/water nanofluids: An experimental study,
815 ANFIS-based model and optimization, J. Mol. Liq. 330 (2021) 115659.
816 [54] G.G. Zhang, G.S. Li, Z.A. Lan, L.H. Lin, A. Savateev, T. Heil, S. Zafeiratos, X.C.
817 Wang, M. Antonietti, Optimizing optical absorption, exciton dissociation, and
818 charge transfer of a polymeric carbon nitride with ultrahigh solar hydrogen
819 production activity, Angew. Chem. Int. Ed. 56(43) (2017) 13445-13449.
820 [55] Q.H. Liang, Z. Li, X.L. Yu, Z.H. Huang, F.Y. Kang, Q.H. Yang, Macroscopic 3D
821 porous graphitic carbon nitride monolith for enhanced photocatalytic hydrogen
822 evolution, Adv. Mater. 27(31) (2015) 4634-4639.
823 [56] J.Z. Jiang, OY. Lei, L.H. Zhu, A.M. Zheng, J. Zou, X.F. Yi, H.Q. Tang,
824 Dependence of electronic structure of g-C_3N_4 on the layer number of its nanosheets:

A study by Raman spectroscopy coupled with first-principles calculations, Carbon 80 (2014) 213-221.

[57] P. Wang, J. Wang, T.S. Ming, X.F. Wang, H.G. Yu, J.G. Yu, Y.G. Wang, M. Lei, Dye-sensitization-induced visible-light reduction of graphene oxide for the enhanced TiO_2 photocatalytic performance, ACS Appl. Mater. Interfaces 5(8) (2013) 2924-2929.

[58] H. Pan, J.M. Sun, J.Y. Liu, Y. Zhang, S.Y. Zhou, Preparation of sulfonated carbon derived from orange peel and its application in esterification, Chem. Phys. Lett. 770 (2021) 138395.

[59] Q.J. Xiang, J.G. Yu, M. Jaroniec, Preparation and enhanced visible-light photocatalytic H-2-production activity of graphene/C_3N_4 composites, J. Phys. Chem. C 115(15) (2011) 7355-7363.

[60] Y. Li, R. Jin, Y. Xing, J. Li, S. Song, X. Liu, M. Li, R. Jin, Macroscopic foam-like holey ultrathin g-C_3N_4 nanosheets for drastic improvement of visible-light photocatalytic activity, Adv. Energy Mater. 6(24) (2016) 1601273.

[61] L.L. Qu, Y.Y. Liu, M.K. Liu, G.H. Yang, D.W. Li, H.T. Li, Highly reproducible Ag NPs/CNT-intercalated GO membranes for enrichment and SERS detection of antibiotics, ACS Appl. Mater. Interfaces 8(41) (2016) 28180-28186.

[62] W.Y. Tang, Y.A. An, K.H. Row, Fabrication of Au nanoparticles embedded holey g-C_3N_4 as SERS substrates for sensitive and reliable detection, Chem. Eng. J. 402 (2020) 126194.

[63] M. Li, Y.T. Li, D.W. Li, Y.T. Long, Recent developments and applications of screen-printed electrodes in environmental assays-A review, Anal. Chim. Acta 734 (2012) 31-44.

[64] Z.W. Yang, X.Q. Xu, X.X. Liang, C. Lei, Y.H. Cui, W.H. Wu, Y.X. Yang, Z. Zhang, Z.Q. Lei, Construction of heterostructured MIL-125/Ag/g-C_3N_4 nanocomposite as an efficient bifunctional visible light photocatalyst for the organic oxidation and reduction reactions, Appl. Catal. B 205 (2017) 42-54.

[65] Y.A. Wei, X. Li, Y.L. Zhang, Y.S. Yan, P.W. Huo, H.Q. Wang, G-C_3N_4 quantum dots and Au nano particles co-modified CeO_2/Fe_3O_4 micro-flowers photocatalyst

for enhanced CO_2 photoreduction, Renew. Energ. 179 (2021) 756-765.

[66] W.G. Fan, M.K.H. Leung, Recent development of plasmonic resonance-based photocatalysis and photovoltaics for solar utilization, Molecules 21(2) (2016) 180.

[67] H.S. Lai, H.D. Zhang, G.K. Li, Y.F. Hu, Bimetallic AgNPs@dopamine modified-halloysite nanotubes-AuNPs for adenine determination using surface-enhanced Raman scattering, Microchim. Acta 188(4) (2021) 127.

[68] N.N. Tri, D.Q. Ho, A.J.P. Carvalho, M.T. Nguyen, N.T. Trung, Insights into adsorptive interactions between antibiotic molecules and rutile-TiO_2 (110) surface, Surf. Sci. 703 (2021) 121723.

[69] A.J. Hallock, P.L. Redmond, L.E. Brus, Optical forces between metallic particles. P. Natl. Acad. Sci. USA. 102(5) (2005) 1280-1284.

[70] X.J. Luo, J.T. Zhu, W. Y. Jia, N.N. Fang, P. Wu, C.X. Cai, J.J. Zhu, Boosting long-range surface-enhanced Raman scattering on plasmonic nanohole arrays for ultrasensitive detection of MiRNA, ACS Appl. Mater. Interfaces 13(15) (2021) 18301-18313.